moment of inertia. The resonant period increases by 4,260 ns when the porous Vycor glass disk in the torsion bob is filled with solid ^{4}He at 62 bar, therefore the supersolid fraction—the fraction of ^{4}He atoms that participate in superflow—is 5 parts in 10^3. On the other hand, if we assume that the χ factor of supersolid is 0.8, the same as that of superfluid in Vycor[18], then the supersolid fraction is 25 parts in 10^3. If we assume that the ^{4}He atoms in the supersolid fraction are uniformly distributed in the pore space and if we neglect interaction between these atoms, then we can use the ideal Bose gas theory to calculate the Bose–Einstein condensation temperature[19]. The calculated transition temperatures are 120 mK and 350 mK, respectively, for supersolid fractions of 5 and 25 parts in 10^3, bracketing the observed transition temperature of 175 mK.

In order to rule out non-supersolid mechanisms for the observed effect, we did a number of control experiments. We made measurements with the same torsional cell with pure solid ^{3}He and with solid ^{4}He diluted with 10, 30, 100, 1,000 and 10,000 p.p.m. of ^{3}He, all pressurized with the same procedures as that for pure ^{4}He, and resulting in a final pressure between 60 and 65 bar. The results of these measurements are shown in Fig. 4. The observed ΔP seen in pure ^{4}He is not seen for solid ^{3}He, and is also not seen for solid mixtures with ^{3}He concentrations exceeding 0.1%. The fact that the effect is not present in ^{3}He, a Fermi system, is reassuring. It is also reasonable that the addition of enough ^{3}He atoms is effective in quenching the supersolid phase. The behaviour found in samples with even lower ^{3}He concentrations is very intriguing. Besides reducing the magnitude of ΔP, the introduction of the minute amount of ^{3}He also broadens the transition and increases the transition temperature.

Figure 4 also shows measurements made with a dummy torsional oscillator consisting of a torsion rod that is identical to the normal torsional cell but with a torsion bob containing a solid brass disk rather than a Vycor glass disk. During measurements, the hole in the torsion rod is pressurized with solid ^{4}He (using the exact same procedure as that for the Vycor torsional cell) to a final pressure of 62 bar. The resonant period is temperature independent, showing no decrease at low temperature, similar to that of the empty cell. This means the effect that we have seen with pure solid ^{4}He and with ^{4}He diluted with small ^{3}He impurities occurs inside the torsion cell, and is not related to changes occurring in the bulk solid helium inside the torsion rod. Owing to the freezing of dislocations, solid helium inside the torsion rod stiffens at low temperature. This stiffening can contribute to the torsional spring constant of the torsion rod[20] and lower the resonant period. We have, however, taken the precaution of using an especially thick (2.2 mm diameter) torsion rod, so that this effect can be ignored. This assumption is confirmed by our measurements with the dummy cell.

It could be argued that solidification inside the Vycor glass is never complete, and that there is a persistent thin liquid film even at 62 bar, 20 bar above the reported solidification pressure. But there are observations that are not consistent with this picture. The temperature dependence of the supersolid is distinctly different from that of a liquid film, and the critical velocity observed for the solid is at least 700 times smaller than that in a film[16]. Figure 4 shows that the introduction of 0.1% of ^{3}He into solid ^{4}He completely eliminates the observed drop in the period. This is in strong contrast to the findings in liquid films. The addition of ^{3}He into a liquid ^{4}He film smoothly decreases the superfluid transition temperature, and a very high concentration of ^{3}He is needed to completely quench the transition[21]. The transition temperature of a pure ^{4}He film at 150 mK was found to decrease to below 20 mK only when the amount of ^{3}He exceeds 20% of all the ^{4}He in the adsorbed film, including that in the amorphous solid layer[21].

In conclusion, the most reasonable interpretation of the observed period drop is that it is a signature of transition into the supersolid state. The microscopic origin of this effect is not understood. We have noted that the solid ^{4}He grown in the Vycor pores is heavily populated with vacancies and defects. It seems that these vacancies may be responsible for enhancing Bose–Einstein condensation of the confined solid ^{4}He into the supersolid phase. ☐

Received 23 September; accepted 14 November 2003; doi:10.1038/nature02220.

1. Kapitza, P. Viscosity of liquid helium below the λ-point. *Nature* **141,** 74 (1938).
2. Penrose, O. & Onsager, L. Bose-Einstein condensation and liquid helium. *Phys. Rev.* **104,** 576–584 (1956).
3. Andreev, A. F. & Lifshitz, I. M. Quantum theory of defects in crystals. *Sov. Phys. JETP* **29,** 1107–1113 (1969).
4. Chester, G. V. Speculations on Bose-Einstein condensation and quantum crystals. *Phys. Rev. A* **2,** 256–258 (1970).
5. Leggett, A. J. Can a solid be "superfluid"? *Phys. Rev. Lett.* **25,** 1543–1546 (1970).
6. Meisel, M. W. Supersolid ^{4}He—An overview of past searches and future possibilities. *Physica B* **178,** 121–128 (1992).
7. Anderson, M. H., Ensher, J. R., Matthews, M. R., Wieman, C. E. & Cornell, E. A. Observation of Bose-Einstein condensation in a dilute atomic vapour. *Science* **269,** 198–201 (1995).
8. Bishop, D. J., Paalanen, M. A. & Reppy, J. D. Search for superfluidity in hcp ^{4}He. *Phys. Rev. B* **24,** 2844–2845 (1981).
9. Levitz, P., Ehret, G., Sinha, S. K. & Drake, J. M. Porous Vycor glass—the micro structure as probed by electron-microscopy, direct energy-transfer, small-angle scattering, and molecular adsorption. *J. Chem. Phys.* **95,** 6151–6161 (1991).
10. Brewer, D. F., Cao, L., Girit, C. & Reppy, J. D. ^{4}He transition in a restricted geometry below and above the bulk solidification pressure. *Physica B* **107,** 583–584 (1981).
11. Cao, L., Brewer, D. F., Girit, C., Smith, E. N. & Reppy, J. D. Flow and torsional oscillator measurements on liquid helium in restricted geometries under pressure. *Phys. Rev. B* **33,** 106–117 (1986).
12. Beamish, J. R., Hikata, A., Tell, L. & Elbaum, C. Solidification and superfluidity of ^{4}He in porous Vycor glass. *Phys. Rev. Lett.* **50,** 425–428 (1983).
13. Molz, E. B. & Beamish, J. R. Freezing and melting of helium in different porous media. *J. Low-Temp. Phys.* **101,** 1055–1077 (1995).
14. Adams, E. D., Uhlig, K., Tang, Y. H. & Haas, G. E. Solidification and superfluidity of ^{4}He in confined geometries. *Phys. Rev. Lett.* **52,** 2249–2252 (1984).
15. Bittner, D. N. & Adams, E. D. Solidification of helium in confined geometries. *J. Low-Temp. Phys.* **97,** 519–535 (1994).
16. Chan, M. H. W., Yanof, A. W. & Reppy, J. D. Superfluidity of thin ^{4}He films. *Phys. Rev. Lett.* **32,** 1347–1350 (1974).
17. Mehl, J. B. & Zimmermann, W. Jr Flow of superfluid helium in a porous medium. *Phys. Rev.* **167,** 214–229 (1968).
18. Berthold, J. E., Bishop, D. J. & Reppy, J. D. Superfluid transition of ^{4}He films adsorbed on porous Vycor glass. *Phys. Rev. Lett.* **39,** 348–352 (1977).
19. Huang, K. *Statistical Mechanics* 2nd edn, 293 (Wiley & Son, New York, 1967).
20. Palaanen, M. A., Bishop, D. J. & Dail, H. W. Dislocation motion in hcp ^{4}He. *Phys. Rev. Lett.* **46,** 664–667 (1981).
21. Csáthy, G. A. & Chan, M. H. W. Effect of ^{3}He on submonolayer superfluidity. *Phys. Rev. Lett.* **87,** 045301 (2001).

Acknowledgements We acknowledge discussions with J. Banavar, J. Beamish, V. Crespi, J. Goodkind, J. Jain, A. Leggett and J. Reppy. This work was supported by the Condensed Matter Physics Program of the National Science Foundation.

Competing interests statement The authors declare that they have no competing financial interests.

Correspondence and requests for materials should be addressed to M.H.W.C. (chan@phys.psu.edu).

Partial order in the non-Fermi-liquid phase of MnSi

C. Pfleiderer[1], **D. Reznik**[3,4], **L. Pintschovius**[3], **H. v. Löhneysen**[1,3], **M. Garst**[2] **& A. Rosch**[2]

[1]*Physikalisches Institut,* [2]*Institut für Theorie der Kondensierten Materie, Universität Karlsruhe, D-76128 Karlsruhe, Germany*
[3]*Forschungszentrum Karlsruhe, Institut für Festkörperphysik, D-76021 Karlsruhe, Germany*
[4]*Laboratoire Léon Brillouin, CEA Saclay, F-91191 Gif-sur-Yvette Cedex, France*

Only a few metallic phases have been identified in pure crystalline materials. These include normal, ferromagnetic and antiferromagnetic metals, systems with spin and charge density wave order, and superconductors. Fermi-liquid theory provides a basis for the description of all of these phases. It has been suggested

that non-Fermi-liquid phases of metals may exist in some heavy-fermion compounds[1,2] and oxide materials[3–6], but the discovery of a characteristic microscopic signature of such phases presents a major challenge. The transition-metal compound MnSi above a certain pressure ($p_c = 14.6$ kbar) provides what may be the cleanest example of an extended non-Fermi-liquid phase in a three-dimensional metal[7–9]. The bulk properties of MnSi suggest that long-range magnetic order is suppressed at p_c (refs 7–12). Here we report neutron diffraction measurements of MnSi, revealing that sizeable quasi-static magnetic moments survive far into the non-Fermi-liquid phase. These moments are organized in an unusual pattern with partial long-range order. Our observation supports the existence of novel metallic phases with partial ordering of the conduction electrons (reminiscent of liquid crystals), as proposed for the high-temperature superconductors[4–6] and heavy-fermion compounds[13].

The identification of novel metallic phases, as opposed to complicated crossover phenomena, has become controversial for a number of reasons. (1) The behaviour is observed in entirely new classes of materials for which little is known in general. (2) The role of dimensionality is unclear. (3) Metallurgical complexities exist, such as chemical segregation and defects. (4) The properties are extremely sensitive to a careful fine-tuning of the experimental conditions. (5) Characteristic energy scales are all of similar magnitude, and cannot be distinguished properly; examples are fluctuations of spin, charge or superconducting order in the high-T_c copper oxides.

The transition-metal compound MnSi is devoid of these complexities. (1) It is a very well-known system, and is perhaps the most extensively studied itinerant-electron magnet apart from iron, cobalt, nickel and chromium. (2) A large body of thermodynamic and microscopic data[10–12,14–20] establish the ground state below the magnetic ordering temperature $T_c = 29.5$ K as a three-dimensional weakly spin-polarized Fermi liquid *par excellence*, with the possible exception of recent high-frequency optical conductivity experiments[21]. (3) As a congruently melting compound, MnSi can be produced at high purity and high crystalline perfection in the cubic B20 structure. (4) At the first-order magnetic quantum phase transition at $p_c = 14.6$ kbar, a discontinuous change from Fermi-liquid behaviour to an extended non-Fermi-liquid (NFL) phase has been inferred from the resistivity[7–9], which is proportional to $T^{1.5}$ for almost three decades in temperature T from around 6 K down to a few mK and for a large pressure range above p_c. This suggests that the novel behaviour does not require careful fine-tuning. (5) Three well-separated energy and length scales can be distinguished in MnSi at all temperatures, pressures and magnetic fields as follows. First, MnSi has a strong tendency to itinerant ferromagnetism on length scales of a few lattice constants, $a = 4.56$ Å, with an ordered moment of about $0.4\,\mu_B$ per formula unit (where μ_B is the Bohr magneton). Second, as the B20 structure lacks an inversion symmetry, weak spin–orbit interactions assume a Dzyaloshinsky–Moriya (DM) form, $\int \mathbf{S}\cdot(\nabla \times \mathbf{S})\,\mathrm{d}\mathbf{r}$, which (being linear in momentum) destabilizes the uniform ferromagnetic order and introduces a well-understood[22,23] helical modulation of a long wavelength 175 Å at ambient pressure. (Here $\mathbf{S}(\mathbf{r})$ is the space dependent magnetization.) Third, in the ordered phase, further spin–orbit interactions induced by the cubic crystalline electric fields lock the direction of the spiral to $\mathbf{Q} = \langle 111 \rangle$, where $\mathbf{S} \perp \mathbf{Q}$ (refs 19, 20, 22, 23). Typical sizes of magnetic domains in the ordered state are 10^4 Å (ref. 20). The locking of the direction of the helix hence represents the weakest scale.

For our study the helical modulation at ambient pressure proves to be crucial, because the corresponding Bragg scattering at $|\mathbf{Q}| = 0.037\,\text{Å}^{-1}$ is confined to a tiny volume of reciprocal space, making it easy to track the magnetic order as a function of pressure. The experiments were made possible through use of a single-crystal sample of exceptional structural perfection, which permits the resolution of the magnetic satellites at high precision. Cold neutron triple-axis diffraction was performed at the Laboratoire Léon Brillouin (LLB), and small-angle neutron scattering (SANS) at the Hahn-Meitner Institut (HMI), Berlin, using a miniature clamp-type pressure cell (see Methods).

At ambient pressure, we observe resolution-limited magnetic Bragg reflections of a coherence length $\xi > 2{,}000$ Å at $\mathbf{Q} = 0.037\,\text{Å}^{-1}$ (111), which are characteristic of conventional three-dimensional long-range order. This is in excellent agreement with previous studies[19,20]. In the temperature versus pressure (T–p) plane, the magnetic ordering temperature of MnSi at ambient pressure, $T_c = 29.5$ K, determined by resistivity and susceptibility measurements[10,11], falls monotonically with pressure, and vanishes at $p_c = 14.6$ kbar in a first-order transition, indicative of a collapse of the static ordered magnetic moments[10] (see Fig. 1). For the pressure range of interest, the lattice constant changes by only a few tenths of a per cent only in agreement with the compressibility[14], and at all pressures the lattice mosaic spread remains unchanged, and is that of an essentially perfect single crystal.

Shown in Fig. 1 is a qualitative illustration of our key result, as we approach and enter the NFL phase. Below a crossover temperature T_0 and even for pressures well above p_c (that is, deep inside the NFL

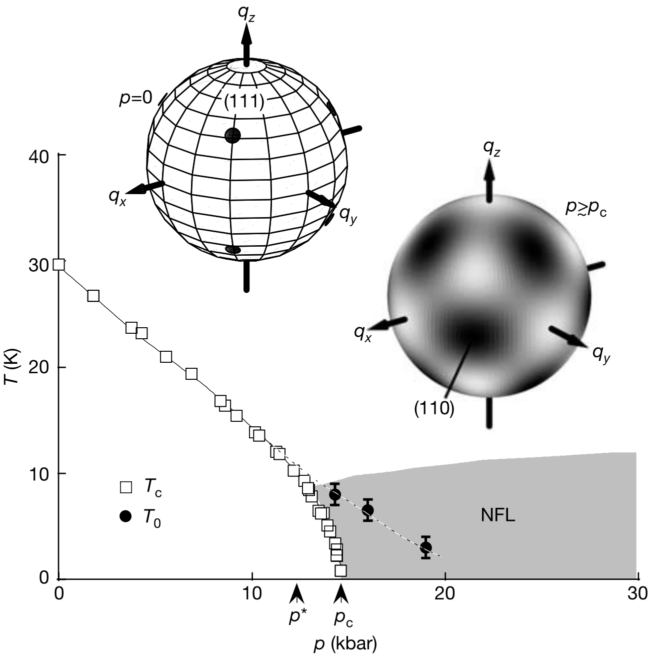

Figure 1 Schematic temperature T versus pressure p phase diagram of MnSi, and qualitative illustration of the scattering intensity characteristic of the magnetic state. Data points of $T_c(p)$ are taken from ref. 10. In the T–p plane, the transition at T_c decreases with increasing pressure and changes from second-order to weakly first-order at $p^* = 12$ kbar, before it disappears above $p_c = 14.6$ kbar. It has been argued that above p_c the non-Fermi-liquid (NFL) resistivity $\rho \propto T^{1.5}$ (which has been observed down to a few mK near p_c) provides evidence of an extended NFL phase (shaded) in a clean three-dimensional metal[7–9]. The insets qualitatively show the location and key features of elastic magnetic scattering intensity in reciprocal space at ambient pressure (left) and at high pressure (right). Data were collected near the [110] lattice Bragg peak. At ambient pressure, resolution-limited magnetic Bragg peaks (indicated by the black dots) are observed at a distance $Q = 0.037\,\text{Å}^{-1}$, characteristic of three-dimensional long-range magnetic order, in perfect agreement with previous work. Note that the size of the dots does not reflect the resolution, and is only chosen for clarity. At high pressure, intensity is observed below a crossover temperature T_0 on the surface of a tiny sphere of radius $Q \approx 0.043\,\text{Å}^{-1}$. The intensity on this surface varies as roughly depicted by the shading, and is highest around ⟨110⟩. In the phase diagram, we show that T_0 decreases with increasing pressure, but remains finite at 19 kbar ($>p_c$), the highest pressure studied.

phase), we observe static magnetic order within the limit of our energy resolution of 50 μeV. This alone is unexpected, because the bulk properties clearly suggest the loss of long-range order at p_c. Moreover, instead of well-defined magnetic Bragg satellites, scattering intensity is found essentially everywhere on the surface of a tiny sphere with radius $Q \approx 0.043\,\text{Å}^{-1}$. The total integrated scattering intensity over the sphere at 1.6 K is of similar magnitude to that at ambient pressure. This is consistent with the observation that the bulk magnetic moment is almost independent of pressure in a polarizing magnetic field of 0.6 T (ref. 12), and suggests that we are seeing the dominant feature of the magnetic state at high pressure.

To explore the distribution of intensity on this sphere, we have performed longitudinal (radial) and transverse (tangential) scans of the magnetic intensity. For longitudinal scans in all directions, we always find resolution-limited correlation lengths $\xi > 2{,}000$ Å, in agreement with long-range longitudinal order. This is illustrated for ⟨110⟩ in Fig. 2a at $p = 14.3$ kbar and in Fig. 2c at $p = 16$ kbar, where the longitudinal width does not change with temperature. In striking contrast, the corresponding transverse scans shown in Fig. 2b and d display a very large angular spread of intensity around ⟨110⟩. For 14.3 kbar, the transverse spread increases somewhat with decreasing temperature, whereas it remains almost constant for 16 kbar. The transverse width is hence not driven thermally as would be expected if there was long-range order at ⟨110⟩ with a transition temperature below our experimental range.

The detailed variation of the peak intensity with temperature for (111) at ambient pressure (Fig. 3a), is typical of a second-order phase transition, in excellent agreement with previous studies[19,20]. At 1.6 K and $p = 14.3$ kbar, only 4% of the peak intensity of ambient pressure is left (inset of Fig. 3a). Slow thermal cycles show hystereses, with $T_{dn} = 2.2$ K in down sweeps and $T_{up} = 4.8$ K in up sweeps. This is consistent with $T_c = 3.3$ K, measured for the unchanged pressure cell in a vibrating sample magnetometer. The hysteresis is also consistent with previous reports of a first-order transition at T_c for $p^* \approx 12\,\text{kbar} < p < p_c$ (ref. 10) and itinerant metamagnetism above p_c (ref. 11) inferred from the uniform susceptibility and resistivity.

With decreasing temperature, longitudinal peak intensity appears for (110) below T_0 (Fig. 3b). In comparison to the sharp phase transition for (111), T_0 rather marks a crossover. Up to 19 kbar, the highest pressure measured, T_0 gradually falls below the onset of the NFL regime (Fig. 1), but remains finite even far above p_c.

For an interpretation of T_0, we note that no corresponding signatures are seen in either the a.c. susceptibility or resistivity. This is surprising because, on the one hand, the magnetic intensity below T_0 is very large and, on the other hand, the electrical resistivity is exceptionally sensitive to the development of static magnetic structures, as seen by its pronounced drop at T_c (refs 7–10) and at the itinerant metamagnetic transition[7,9]. A possible

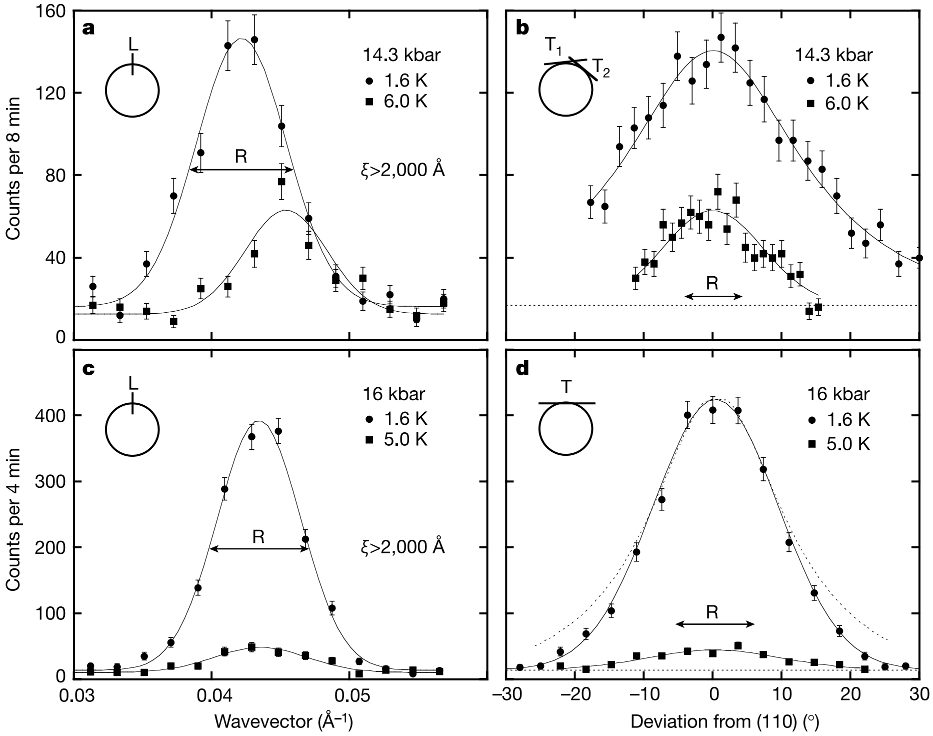

Figure 2 Longitudinal (L) and transverse (T) scans of the magnetic scattering intensity with respect to (110). Data are shown for 14.3 kbar (**a**, **b**), just below p_c, and 16 kbar (**c**, **d**), well above p_c. The direction of the scans with respect to a cross-section of the spherical surface is depicted in the top left corner of each panel. Note that the data at 14.3 kbar and 16 kbar are taken on two different samples with different scattering planes, thus underscoring the reproducibility of the effects (see Methods). The arrow marked R shows the instrumental resolution. **a**, Typical longitudinal scan along (110) at $p = 14.3$ kbar for 1.6 K and 6.0 K. The magnitude of $|\mathbf{Q}| \approx 0.043\,\text{Å}^{-1}$ corresponds to a wavelength of 150 Å. The resolution-limited coherence length $\xi > 2{,}000$ Å is characteristic of long-range order. For different directions of the longitudinal scans, the intensity peaks at the same value of $|\mathbf{Q}|$, that is, the intensity lies on the surface of a sphere. **b**, Typical transverse scan at $p = 14.3$ kbar with respect to (110) in the plane spanned by (110) and (111). The data shown is composed of two transverse scans T_1 and T_2 that were chosen such that the data displays the intensity along the arc for fixed $|\mathbf{Q}|$ with respect to (110). With decreasing temperature, the angular spread slightly increases. The large transverse width does not correspond to a short transverse correlation length, as discussed in the text. **c**, Typical longitudinal scan along (110) at $p = 16$ kbar for 1.6 K and 5.0 K. As for 14.3 kbar, the longitudinal width is resolution-limited. **d**, Typical transverse scan at $p = 16$ kbar with respect to (110) as above. Data were recorded along a single straight trace T. The dashed line is the variation of the intensity along a transverse arc for fixed $|\mathbf{Q}|$ (compare with Fig. 2b) calculated from the experimental data. Within the errors for the calculated curve, the transverse spread at 14.3 kbar and 16 kbar is the same. At 16 kbar, the transverse spread is roughly independent of temperature.

solution of this apparent contradiction is that the quasi-static magnetic structure seen in neutron diffraction below T_0 in fact fluctuates on the timescale relevant for transport, and that above T_0 the magnetic structures fluctuate too rapidly for large pressures and temperatures to be captured by our quasi-elastic resolution of 50 μeV. We believe that these fluctuations are the key feature of the entire NFL phase. However, studies of finely powdered MnSi may indicate that local moments exist below T_0 (ref. 24) which are static on timescales relevant for nuclear magnetic resonance (NMR) experiments. It will be a major challenge for future inelastic neutron experiments (and complementary NMR investigations) to clarify how T_0 changes with neutron energy, and whether its pressure dependence is controlled by a quantum phase transition of a subtle magnetic order at an extrapolated pressure of ~22 kbar, where T_0 might vanish (Fig. 1).

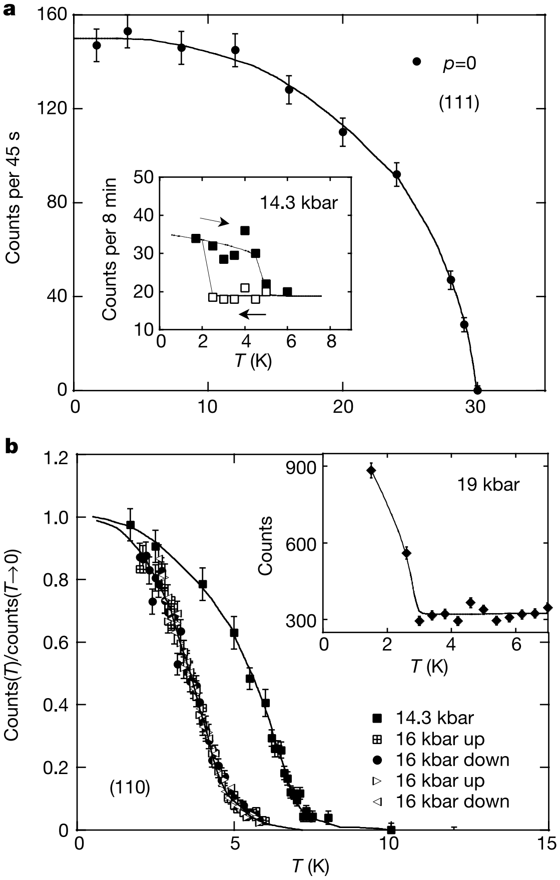

Figure 3 Temperature dependence of the longitudinal peak intensity for scans along (111) and (110) at various pressures. **a**, Temperature dependence of the satellite along (111). At ambient pressure, a second-order phase transition is observed in accordance with previous work. The inset shows the temperature dependence at 14.3 kbar, just below p_c. Taking differences of sample volume into account, only 4% of the peak intensity is left at 1.6 K. Thermal cycles display hysteresis, where T_c is in general agreement with the signature in the bulk magnetization of the same pressure cell and sample measured in a vibrating sample magnetometer. **b**, Temperature dependence for the peak intensity along (110). At 14.3 kbar, a gradual crossover below $T_0 \approx 8$ K is observed. Note that the quasi-static intensity for this satellite already appears above T_c. NFL resistivity is observed roughly between T_0 and T_c as indicated by the grey shading in Fig. 1 above T_c. At 16 kbar, the crossover temperature is shifted to $T_0 \approx 6$ K. No hysteresis is observed in thermal cycles. The inset displays the temperature dependence of the peak intensity along (110) at 19 kbar where the crossover is shifted to $T_0 \approx 3$ K. Note that the temperature-dependent data shown in the inset were taken on a small-angle spectrometer, causing a higher background. To improve statistics, data at 19 kbar were also recorded in a field-cooled state.

Before our study it was generally believed that the static amplitude of the magnetic moment (and therefore also the spiral itself) disappears at $p_c = 14.6$ kbar (refs 7–12). In contrast, the pronounced longitudinal order shows that the helix continues to exist well above p_c with a large integrated scattering intensity. For different directions of the longitudinal scans, the intensity peaks at the same value of $|\mathbf{Q}|$; that is, the intensity lies on a sphere. Hence the transverse width must not be mistaken for short-range transverse magnetic correlations, but results from a considerable variation of the directions of the spirals. This clearly establishes that the magnetic quantum phase transition seen in the bulk properties at p_c results from an unlocking of the spiral from $\langle 111 \rangle$, driven by the weakest of the three characteristic scales discussed above.

The variations of the direction of the spirals might exist in any combination of two extremes. First, the magnetic structure may break up into a multi-domain state where the direction of the spiral varies strongly from domain to domain, and the helix may end abruptly between domains. This implies the proliferation of so-called topological defects, such as domain walls or line defects. We speculate that either the structure of those defects, the quantum fluctuations within a domain or their mutual frustration prevents the direction of the helix from locking. Second, a situation might exist where the spirals remain intact, but meander such that they do not exhibit strict directional order. Compared to the first model, such a state is defined by the absence of certain types of topological defects, and is said to develop 'topological order'. Lammert, Rokhsar and Toner[25] showed that such topological order may exist in the isotropic phase of a nematic liquid crystal when the energy costs of forming disclinations are unfavourably high.

Quite generally, it is interesting to compare liquid crystals with the partial order we observe here—to our knowledge, for the first time—as a property of the conduction electrons in a metal. Owing to the lack of inversion symmetry, the properties of MnSi are related to cholesteric liquid crystals[26]. In these cholesterics, a helical phase undergoes a sequence of phase transitions to so-called 'blue phases', which are characterized by complex patterns of the order parameter woven from topological defects of the underlying chiral helices[25]. In our context, the blue phase III (also known as 'blue fog') is particularly interesting as it exhibits complex local order but no long-range order[27].

The unlocking of the spiral implies an entirely surprising microscopic origin of the NFL phase, anticipated neither experimentally nor theoretically. The identification of the corresponding low-lying excitations and their connection with the $T^{1.5}$ resistivity therefore defines a major challenge for future theoretical and experimental work. Within a partially ordered state, unconventional scattering mechanisms may, for instance, result from (pseudo-) Goldstone modes connected with fluctuations of the direction of the spirals, from internal excitations of domain walls[28] or other topological defects, from highly frustrated glassy magnetic configurations[29], from hidden quantum criticality, or from Berry phases of electrons moving on top of spin textures.

Partial electronic order as a general phenomenon of new states of matter in metals has been extensively studied theoretically in the context of the high-T_c copper oxides[4–6] and heavy-fermion systems[13]. The clear evidence for microscopic partial order in combination with the pronounced macroscopic NFL behaviour and well-separated energy and length scales makes MnSi unique, and provides strong experimental support for the genuine existence of such phases in extremely clean systems. □

Methods

Neutron diffraction

Neutron diffraction experiments were carried out on the cold thermal neutron triple-axis spectrometer 4F1 at the LLB. A feasibility study was also carried out at the SANS spectrometer V4 at the HMI. Use of a triple-axis spectrometer allowed a significant reduction of the diffuse scattering by the miniature pressure cell described below. On the triple-axis spectrometer, we achieved a high resolution in energy better than 50 μeV. For most of the work reported here, the spectrometer was used in an elastic mode where the initial wavevector was chosen as $k_i = 1.2$ Å. Data were collected near the [110] lattice Bragg point. The spectrometer 4F1 permits scans on a cartesian grid only, so that the transverse spread could only be studied in scans tangential (T) to the sphere of intensity shown in Fig. 1 (see also Fig. 2 legend). The resolution function was determined at the [110] nuclear Bragg peak, and is marked in the plots as R. For the experiments, the miniature pressure cell was mounted on a so-called orange cryostat, for minimum temperatures of 1.6 K. The data collected at the SANS spectrometer V4 reproduce the triple-axis data in the region of data overlap. We follow the usual convention where [..] denotes reciprocal lattice points, (..) a particular direction in reciprocal space and ⟨..⟩ the family of all equivalent directions in reciprocal space.

High-pressure techniques

High pressures were generated with a miniature clamp cell (outer diameter 12 mm) made of Cu:Be using standard PTFE sealing caps and Fluorinert as pressure transmitter. The diameter of the cylindrical samples was smaller than the inner diameter of the PTFE sealing caps by a few tenths of a millimetre. The samples were left floating free in the pressure medium to avoid the effects of differential contraction by a sample mount. Two pressure cells were prepared with a sample each, where the ⟨110⟩ and ⟨111⟩ axes were, respectively, parallel to the cylinder axis to save experiment time and to test for reproducibility. The lattice mosaic spread was found to be unchanged for both samples at all pressures studied. The pressure technique is identical to that used in a large number of studies of bulk properties of, for example, the resistivity, magnetization and quantum oscillatory phenomena, and was previously used in similar neutron diffraction studies[30]. None of these studies indicated any hints of non-hydrostatic pressure components. However, we observe a trend for the domains in the scattering plane to be populated most strongly, that is perpendicular to the vertical axis of the pressure cell. This may be a consequence of tiny non-hydrostatic components that freeze into the pressure transmitter that we were not able to detect in the lattice mosaic or lattice form factor. For the two pressure cells, the longitudinal and transverse spread described in the text is reproducibly the same, clearly establishing that the effects are intrinsic to the sample and not caused by any tiny non-hydrostaticities. The pressure was consistently determined from (1) the change of the lattice constant, (2) the superconducting transition of Sn and (3) the bulk magnetic transition measured in a vibrating sample magnetometer when $p < p_c$.

Sample preparation and quality

The single-crystal samples investigated here were grown by r.f. induction of zone-refined high-purity starting materials on a water-cooled Cu-crucible in an ultrahigh-vacuum environment. The resulting ingots were annealed for 2 weeks near the melting point. Single-crystal samples were oriented by Laue X-ray diffraction, and cut by low-power spark erosion. The samples investigated have a tiny, resolution-limited mosaic spread $\eta \ll 0.2°$, which compares with industrial quality silicon single crystals and is orders of magnitude smaller than typically found in intermetallic compounds. The very low value of η underscores the exceptional intrinsic spread around ⟨110⟩ of the magnetic state above p_c.

Received 30 September; accepted 14 November 2003; doi:10.1038/nature02232.

1. Chandra, P., Coleman, P., Mydosh, J. A. & Tripathi, V. Hidden orbital order in the heavy fermion metal URu_2Si_2. *Nature* **417,** 831–834 (2002).
2. Grosche, F. M. G. *et al.* Anomalous low temperature states in $CeNi_2Ge_2$ and $CePd_2Si_2$. *J. Phys. Condens. Matter* **12,** L533–L540 (2000).
3. Dagotto, E., Hotta, T. & Moreo, A. Colossal magnetoresistant materials: The key role of phase separation. *Phys. Rep.* **344,** 1–153 (2001).
4. Kivelson, S. A. *et al.* How to detect fluctuating order in the high-temperature superconductors. *Rev. Mod. Phys.* **75,** 1201–1241 (2003).
5. Sachdev, S. Order and quantum phase transitions in the cuprate superconductors. *Rev. Mod. Phys.* **75,** 913–932 (2003).
6. Zaanen, J. *et al.* The geometric order of stripes and Luttinger liquids. *Phil. Mag. B* **81,** 1485–1531 (2001).
7. Pfleiderer, C., Julian, S. R. & Lonzarich, G. G. Non-Fermi liquid nature of the normal state of itinerant-electron ferromagnets. *Nature* **414,** 427–430 (2001).
8. Pfleiderer, C. The non-Fermi liquid puzzle of MnSi at high pressure. *Physica B* **328,** 100–104 (2003).
9. Doiron-Leyraud, N. *et al.* Fermi-liquid breakdown in the paramagnetic phase of a pure metal. *Nature* **425,** 595–599 (2003).
10. Pfleiderer, C., McMullan, G. J., Julian, S. R. & Lonzarich, G. G. Magnetic quantum phase transition in MnSi under hydrostatic pressure. *Phys. Rev. B* **55,** 8330–8338 (1997).
11. Thessieu, C. *et al.* Field dependence of the magnetic quantum phase transition in MnSi. *J. Phys. Condens. Matter* **9,** 6677–6687 (1997).
12. Koyama, K., Goto, T., Kanomata, T. & Note, R. Observation of an itinerant metamagnetic transition in MnSi under high pressure. *Phys. Rev. B* **62,** 986–991 (2000).
13. Barzykin, V. & Gorkov, L. P. Possibility of nontrivial magnetic order by elastic neutron scattering. *Phys. Rev. Lett.* **70,** 2479–2482 (1993).
14. Fawcett, E., Maita, J. P. & Wernick, J. H. Magnetoelastic and thermal properties of MnSi. *Int. J. Magn.* **1,** 29–34 (1970).
15. Bloch, D., Voiron, J., Jaccarino, V. & Wernick, J. H. The high field–high pressure magnetic properties of MnSi. *Phys. Lett. A* **51,** 259–291 (1975).
16. Ishikawa, Y. *et al.* Paramagnetic spin fluctuations in the weak itinerant-electron ferromagnet MnSi. *Phys. Rev. B* **31,** 5884–5893 (1985).
17. Yasuoka, H., Jaccarion, V., Sherwood, R. C. & Wernick, J. H. NMR and susceptibility studies of MnSi above T_c. *J. Phys. Soc. Jpn* **44,** 842–849 (1978).
18. Taillefer, L., Lonzarich, G. G. & Strange, P. The band magnetism of MnSi. *J. Magn. Magn. Mater.* **54–57,** 957–958 (1986).
19. Ishikawa, Y. & Arai, M. Magnetic phase diagram of MnSi near critical temperature studied by neutron small angle scattering. *J. Phys. Soc. Jpn* **53,** 2726–2733 (1984).
20. Lebech, B. in *Recent Advances in Magnetism of Transition Metal Compounds* (eds Kotani, A. & Suzuki, N.) 167–178 (World Scientific, Singapore, 1993).
21. Mena, F. P. *et al.* Heavy carriers and non-Drude optical conductivity in MnSi. *Phys. Rev. B* **67,** 241101(R) (2003).
22. Bak, P. & Jensen, M. H. Theory of helical magnetic structures and phase transitions in MnSi and FeGe. *J. Phys. C* **13,** L881–L885 (1980).
23. Nakanishi, O., Yanase, A., Hasegawa, A. & Kataoka, M. The origin of the helical spin density wave in MnSi. *Solid State Commun.* **35,** 995–998 (1980).
24. Thessieu, C. *et al.* Pressure effect on MnSi: An NMR study. *J. Magn. Magn. Mater.* **177–181,** 609–610 (1998).
25. Lammert, P. E., Rokhsar, D. S. & Toner, J. Topology and nematic ordering. *Phys. Rev. Lett.* **70,** 1650–1653 (1993).
26. Wright, D. C. & Mermin, N. D. Crystalline liquids: The blue phases. *Rev. Mod. Phys.* **61,** 385–432 (1989).
27. Koistinen, E. P. & Keyes, P. H. Light-scattering study of the structures of blue phase III. *Phys. Rev. Lett.* **74,** 4460–4463 (1995).
28. Vonsovskij, S. V. *Magnetism* Vol. 2, Part 3 (Wiley, New York, 1974).
29. Mydosh, J. *Spin Glasses: An Experimental Introduction* (Taylor and Francis, London, 1993).
30. Huxley, A. *et al.* Co-existence of superconductivity and ferromagnetism in actinide compounds. *J. Phys. Condens. Matter* **15,** S1945–S1956 (2003).

Acknowledgements We acknowledge discussions with P. Böni, A. N. Bogdanov, E. Dormann, B. Fåk, P. C. Howell, B. Keimer, B. Lebech, G. G. Lonzarich, I. Mazin, A. J. Millis, K.-H. Müller, J. Mydosh, J. Kübler, B. Rössli, S. Sachdev, S. S. Saxena, J. Schmalian, Q. Si, M. Turlakov, U. Rössler, M. Vojta, P. Wölfle and J. Zaanen. Help with the experiments from M. Uhlarz, B. Hennion, J. Haug, E. Garcia-Matres and the staff of the Laboratoire Léon Brillouin (Saclay) and the Hahn-Meitner Institut (Berlin), respectively, is also acknowledged. This work was supported by the Deutsche Forschungsgemeinschaft, the Helmholtz Gemeinschaft and the European Science Foundation under FERLIN.

Competing interests statement The authors declare that they have no competing financial interests.

Correspondence and requests for materials should be addressed to C.P. (Christian.Pfleiderer@physik.uni-karlsruhe.de).

Observational evidence of a change in radiative forcing due to the indirect aerosol effect

Joyce E. Penner[1], **Xiquan Dong**[2] **& Yang Chen**[1]

[1] *Department of Atmospheric, Oceanic, and Space Sciences, University of Michigan, Ann Arbor, Michigan 48109-2143, USA*
[2] *Department of Atmospheric Science, University of North Dakota, Grand Forks, North Dakota 58202-9006, USA*

Anthropogenic aerosols enhance cloud reflectivity by increasing the number concentration of cloud droplets, leading to a cooling effect on climate known as the indirect aerosol effect. Observational support for this effect is based mainly on evidence that aerosol number concentrations are connected with droplet concentrations, but it has been difficult to determine the impact of these indirect effects on radiative forcing[1–3]. Here we provide observational evidence for a substantial alteration of radiative fluxes due to the indirect aerosol effect. We examine the effect of aerosols on cloud optical properties using measurements of aerosol and cloud properties at two North American sites that span polluted and clean conditions—a continental site in Oklahoma with high aerosol concentrations, and an Arctic site in Alaska with low aerosol concentrations. We determine the cloud optical depth required to fit the observed shortwave downward surface radiation. We then use a cloud parcel model to simulate the cloud optical depth from observed aerosol properties due to the indirect aerosol effect. From the good agreement between the simulated indirect aerosol effect and observed surface radiation,